NATURAL SCIENCE REVIEW **00** 00 (2026)
nsr.jinr.int

In situ performance of the Vertex Silicon Plane in the BM@N experiment during Run 9

D. Dementev*[1], M. Shitenkov[1], A. Kolozhvari[1], V. Leontyev[1,2], A. Sheremetev[1], D. Andreev[1], R. Arteche Diaz[1,3], D. Baranov[4], C. Ceballos Sanchez[1], I. Gabdrakhmanov[1], I. Gorelikov[1], T. Lygdenova[1], I. Osokin[1], S. Reyes Peña[1,5], I. Rufanov[1], E. Tsapulina[1], A. Voronin[1], and Yu. Murin[1]

[1] *Veksler and Baldin Laboratory of High Energy Physics, Joint Institute for Nuclear Research, Dubna, Moscow Region, Russia;*
[2] *Moscow State University, Moscow, Russia;*
[3] *Center of Technological Applications and Nuclear Development, Havana, Cuba;*
[4] *Meshcheryakov Laboratory of Information Technologies, Joint Institute for Nuclear Research, Dubna, Moscow Region, Russia;*
[5] *Higher Institute of Technologies and Applied Sciences, Havana University, Havana, Cuba.*

Abstract

The Vertex Silicon Plane (VSP) was commissioned and operated for the first time as the most upstream tracking station of the Baryonic Matter at Nuclotron (BM@N) experiment at the NICA accelerator complex during Run 9. The station consisting of six double-sided silicon microstrip modules based on the CBM–BM@N detector technology was installed about 8 cm downstream from the target inside the SP-41 analyzing magnet.

The in situ module performance was characterized in terms of the signal-to-noise ratio, time resolution, and Lorentz drift in the magnetic field. The most probable cluster signal-to-noise ratio ranges from 15.5 to 33.2, while the time resolution relative to the trigger pulse is about 12 ns. The tracking performance was evaluated using track–hit residuals and hit-matching efficiency; two independent reference configurations based on the Forward Silicon Detector (FSD) and Gas Electron Multiplier (GEM) tracking systems give consistent efficiencies of about 95%.

The contribution of the VSP to the BM@N tracking performance was further studied through the transverse track impact parameter and the reconstruction of short VSP–GEM tracklets. Owing to its position close to the target and its coverage at large polar angles, the VSP provides an additional near-target tracking point and makes it possible to extend the geometrical acceptance beyond that of the FSD- and GEM-based central tracking system.

Keywords: Silicon microstrip detectors, particle tracking detectors, solid-state detectors, detector performance

*Corresponding author e-mail address: dementiev@jinr.ru

https://doi.org/doi/number

Received: XX Month Year; Revised: XX Month Year; Accepted: XX Month Year; Published: XX Month Year
Copyright: © by the author(s), 2026, under license to Joint Institute for Nuclear Research. This article is an open access article distributed under the terms and conditions of the Creative Commons Attribution-NonCommercial 4.0 International license (CC BY-NC License 4.0).

1. Introduction

1.1. The BM@N experiment

The Baryonic Matter at Nuclotron (BM@N) is a fixed-target experiment at the Nuclotron-based Ion Collider fAcility (NICA) in Dubna, Russia. It is designed to study strongly interacting matter produced in heavy-ion collisions at beam kinetic energies up to 4.5 AGeV [1]. The detector is optimized for charged-particle reconstruction in the forward-rapidity region. A detailed description of the BM@N spectrometer is given in Ref. [2].

The central tracking system (CTS) is located inside the SP-41 large-aperture warm dipole analyzing magnet. It combines four Forward Silicon Detector (FSD) stations based on double-sided silicon microstrip sensors followed by seven Gas Electron Multiplier (GEM) tracking planes. In Run 9, the system was complemented by the Vertex Silicon Plane (VSP), installed upstream of the FSD and GEM stations.

The VSP consists of six CBM–BM@N-type double-sided silicon strip detector (DSSD) modules developed for the large-acceptance Silicon Tracking System of the BM@N experiment [1]. A primary goal of the first VSP commissioning in BM@N was to demonstrate the integration of its data-driven readout into the BM@N data-acquisition system (DAQ). The integration was evaluated through the time correlation of VSP hits with accepted BM@N triggers and their spatial consistency with independently reconstructed tracks.

The VSP provides a space-point measurement close to the target for particles emitted at polar angles of approximately 25°–52°. This angular region is only weakly covered by the FSD stations, whereas the VSP acceptance overlaps that of the first GEM stations, enabling track reconstruction towards the midrapidity region (see Sec. 2.3).

Figure 1 shows the configuration of the central tracking system for Run 9. The incoming beam was measured by the Silicon Beam Tracker (SiBT), located upstream of the target [3]. In this analysis, the SiBT information provides an independent beam constraint used for primary-track selection and for alignment.

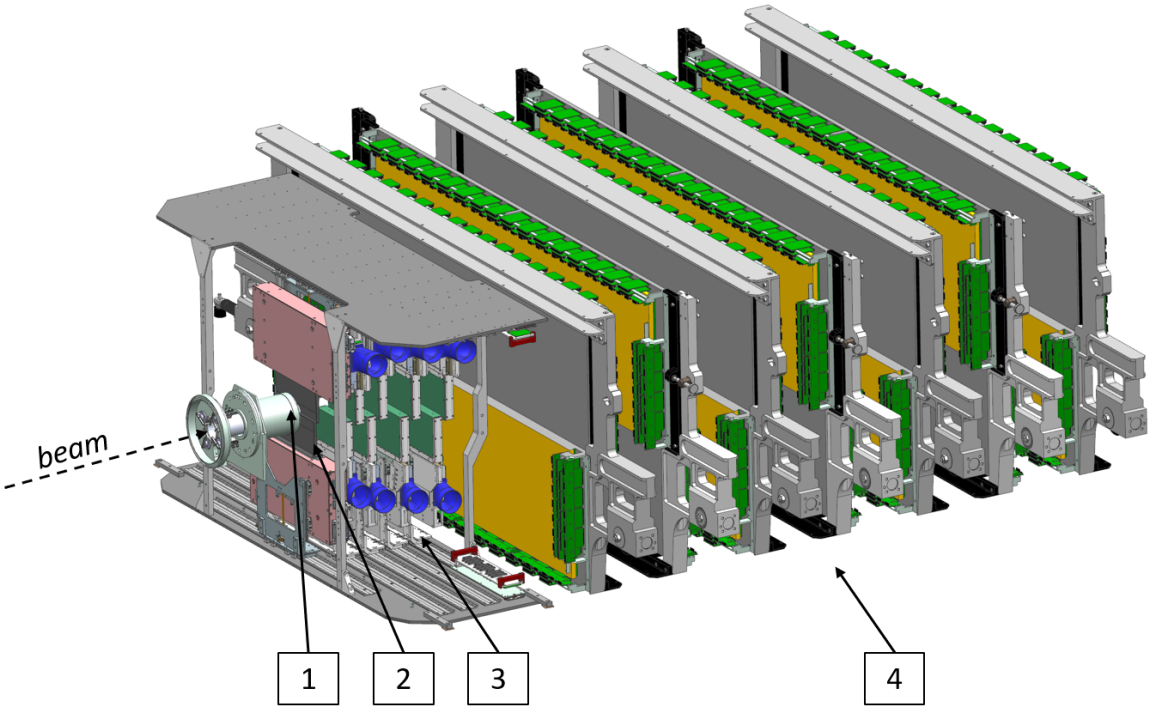


Figure 1. CAD view of the configuration of the central tracking system (CTS) for Run 9 inside the SP-41 dipole magnet. The beam direction is indicated by the dashed arrow. The numbered elements denote: 1 – target chamber, 2 – VSP station, 3 – FSD stations, and 4 – GEM tracking planes. The beam pipe is not shown.

The main tracking-detector parameters are summarized in Table 1. The FSD and GEM systems are described in Ref. [2].

Table 1. Parameters of the tracking detectors of the CTS. The effective pitch in the second coordinate is derived from the strip pitch and the corresponding stereo angle.

Detector	Planes	Strip pitch (X), mm	Effective pitch (Y), mm	Active area, m^2	Channels, $\times 10^3$
VSP	1	0.058	0.44	0.021	12
FSD	4	0.095	2.36	0.307	54
GEM	7	0.80	3.1	9.58	87

1.2. VSP detector

The VSP consists of six double-sided silicon microstrip modules arranged in two half-stations around the vacuum beam pipe. One of the half-stations is shown in Fig. 2. The sensors are located 7.4–8.5 cm downstream from the target, covering polar angles of approximately 23°–52°. The lower limit of the angular acceptance is defined by the central opening for the beam pipe.

The module layout and strip orientations are shown in Fig. 3(a). The average material budget in the sensitive area is about 0.8% of a radiation length (X_0), with local variations due to the module frames and support structures, as shown in Fig. 3(b).

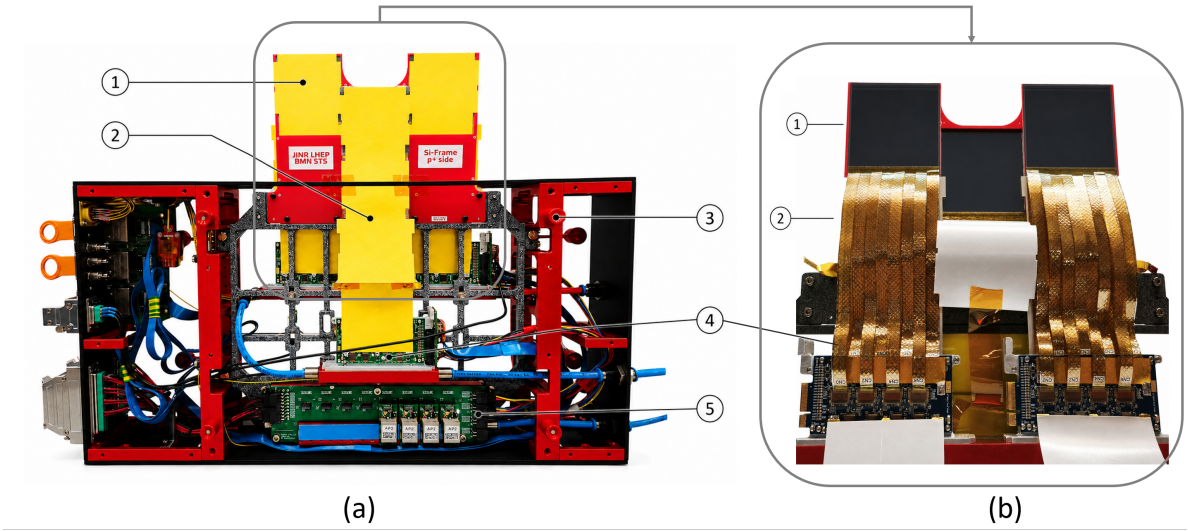


Figure 2. Photographs of one VSP half-station. (a) Half-station before installation of the final shielding covers and positioning mechanics. (b) Enlarged view of the marked DSSD-module region with the microcable stacks exposed. The same numbering is used in both panels: 1 – double-sided silicon strip detector (DSSD) modules; 2 – microcable stacks, covered by aluminum shielding; 3 – alignment-mark seats; 4 – front-end boards with STS/MUCH-XYTER ASICs; 5 – power board with magnetic-field-resistant DC/DC converters.

The VSP modules were assembled at JINR as part of the first batch produced for the wide-aperture Silicon Tracking System of the BM@N experiment [4]. Each module incorporates a double-sided silicon strip sensor with dimensions of 62×62 mm^2, a sensitive area of about 60×60 mm^2, and a thickness of 320 μm. Each sensor side contains 1024 strips with a pitch of 58 μm. The stereo angle between the strip directions on the two sides is 7.5°, resulting in an effective two-dimensional pitch of approximately 58 μm $\times$ 440 μm.

Signals from the strips are routed to the front-end boards through low-mass aluminum–polyimide microcables [4] and read out with STS/MUCH-XYTER (SMX) ASICs [6]. The technological workflow of DSSD module assembly and quality assurance is described in detail in Ref. [5]. The module performance was validated before installation in BM@N in proton-beam tests at the SC-1000 synchrocyclotron in Gatchina [7, 8].

2. Experimental conditions

2.1. Integration of the VSP readout into the BM@N DAQ

The VSP readout is based on the data-driven architecture derived from that developed for the Silicon Tracking System [9, 10]. The front-end electronics uses SMX ASICs operating in a data-driven mode and transmitting zero-suppressed hit frames. A hit is generated independently in each readout channel when the signal amplitude exceeds the preset threshold of the lower ADC comparator. Each VSP hit frame contains time-stamp and amplitude information.

The SMX front-end operates continuously and does not receive an event trigger. The selection of VSP hits is therefore performed in the backend electronics. Incoming BM@N trigger signals are assigned time stamps, which are compared with the time stamps of the continuous VSP hit stream. Hits falling within a 2 μs time window around the trigger time were selected.

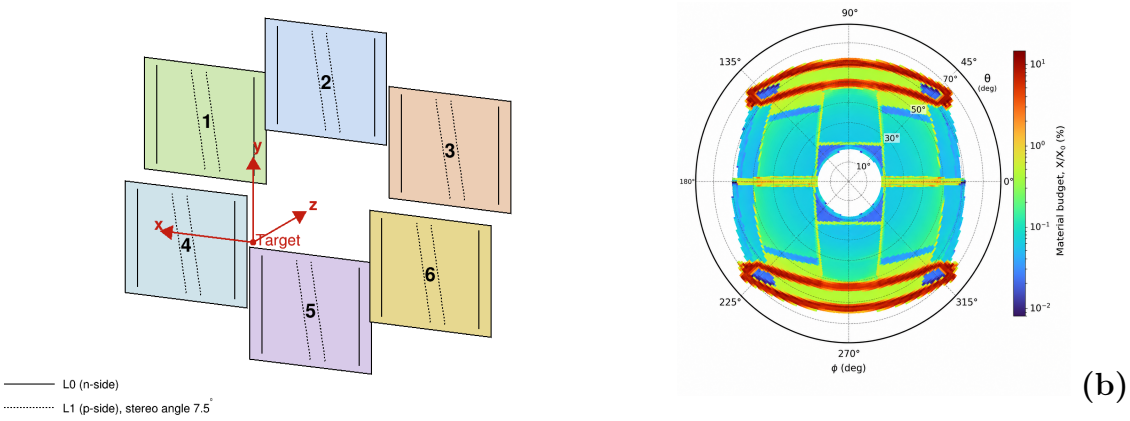


Figure 3. VSP geometry and material distribution. (a) Layout of the six VSP modules obtained from the Run 9 ROOT geometry. The coordinate axes and module numbering are shown. Solid and dashed lines schematically indicate the strip directions on the n-side (L0) and p-side (L1), respectively. (b) Material-budget distribution of the VSP station in polar coordinates, including the silicon modules, module frames, and supporting structures. The radial coordinate corresponds to the polar angle θ, while the azimuthal coordinate is ϕ. The color scale shows the integrated material budget X/X_0.

At the server level, the VSP readout software performs data processing, online monitoring, and interaction with the common BM@N DAQ. The selected VSP data are packed in the MPDRawData format [9] and transferred to the BM@N Event Builder.

2.2. Data-taking conditions

Run 9 data taking lasted from 17 January to 4 April 2026. During this period, the VSP station operated without critical failures affecting the mechanics, cooling, or readout chain.

The sensors were biased at 100 V, and the discriminator thresholds were set to approximately 6×10^3 electrons. Under these conditions, the full-system noise-hit rate measured without beam in data-driven mode was about 1 kHz, corresponding to a probability of approximately 0.2% for a random noise hit within a 2 μs trigger window.

Water cooling was used to stabilize the front-end electronics during operation at temperatures up to 40°C. Owing to the low sensor leakage currents and the sensor power dissipation of about 0.1 mW, no dedicated sensor cooling was required. The sensors were cooled mainly by natural convection and heat exchange with the water-cooled radiators. Under these conditions, the sensor temperature was typically about 25°C, while the ambient temperature varied from approximately 25°C to 37°C.

The performance results presented below are based on two 3.0 AGeV Xe+Sn datasets. A calibration dataset was recorded without magnetic field and a physics dataset was recorded with the nominal BM@N magnetic field.

2.3. Data analysis

The following coordinate and angular conventions are used throughout the analysis. The z axis is directed along the beam, while x and y are the transverse coordinates oriented perpendicular and parallel to the magnetic field direction, respectively, as shown in Fig. 3(a). Track directions are parameterized by the slopes $t_x = dx/dz$ and $t_y = dy/dz$.

The polar angle θ is defined as the angle between the particle direction and the beam axis z. For detector-response studies, the track incidence angle α_s is defined separately for each sensor side in the plane orthogonal to the corresponding strip direction. The two incidence angles are denoted α_{L0} for the n-side (L0) and α_{L1} for the p-side (L1).

The angular acceptance of the VSP relative to the first FSD and GEM stations is shown in Fig. 4. The VSP has only a limited geometrical overlap with the first FSD station, whereas its overlap with the first GEM stations is substantially larger. Consequently, several complementary tracking configurations were used for the detector-performance study.

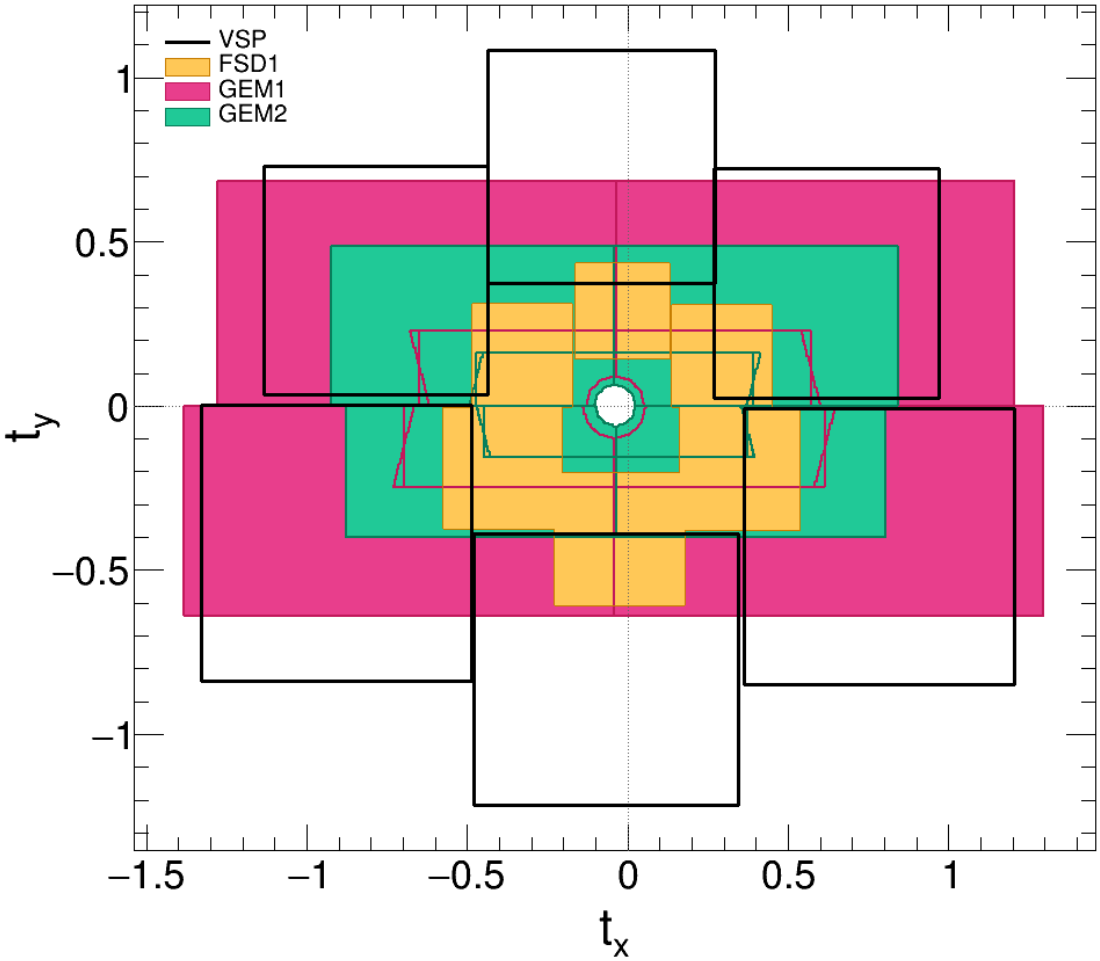


Figure 4. Angular acceptance of the VSP, FSD1, GEM1, and GEM2 in the (t_x, t_y) plane.

Raw data were decoded using the BmnRoot framework, which is based on FairRoot [11]. CTS tracks were reconstructed with the regular offline tracking procedure. Track candidates were built with the Vector Finder toolkit [12] and fitted using a Kalman-filter procedure [13]. These tracks were used for the track impact-parameter study.

The primary vertex used in the analysis was reconstructed with the standard BM@N Kalman-based vertex-fitting procedure [14].

For alignment and geometrical cross-checks, a separate reference was used, based on the target reference point reconstructed with the SiBT together with measurements in the first GEM station. This configuration provides the maximum angular coverage. The alignment procedure and the resulting constants are documented in BM@N internal reports [15, 16].

To extend track reconstruction towards midrapidity, short VSP–GEM tracklets were also constructed using the three-dimensional primary-vertex point, one VSP hit, and measurements in the first two GEM stations. These tracklets exploit the large geometrical overlap between the VSP and the first GEM stations and extend the tracklet acceptance beyond that of the CTS.

3. Results

3.1. Detector response and in situ performance

3.1.1. Time resolution

The VSP time resolution was evaluated from the distribution of VSP hit time stamps relative to the time stamp assigned by the VSP readout to the trigger pulse.

The amplitude dependence of the hit time shown in Fig. 5(a) was fitted using the parameterization described in Ref. [8]; the fitted parameters were then used for the time-slewing correction. After the correction, the hit–trigger time distribution exhibits a well-defined peak, as shown in Fig. 5(b). A Gaussian fit gives a standard deviation of $\sigma_t = 11.8$ ns. This value represents the time resolution of the VSP relative to the trigger pulse and includes contributions from the front-end time stamping, residual time-slewing effects, trigger-reference jitter, and readout synchronization.

The observed time correlation demonstrates the successful matching of the free-streaming VSP data with the BM@N trigger stream. The achieved time resolution is sufficient for selecting in-time VSP hits within the 2 μs trigger window and suppressing out-of-time hits in the data-driven readout.

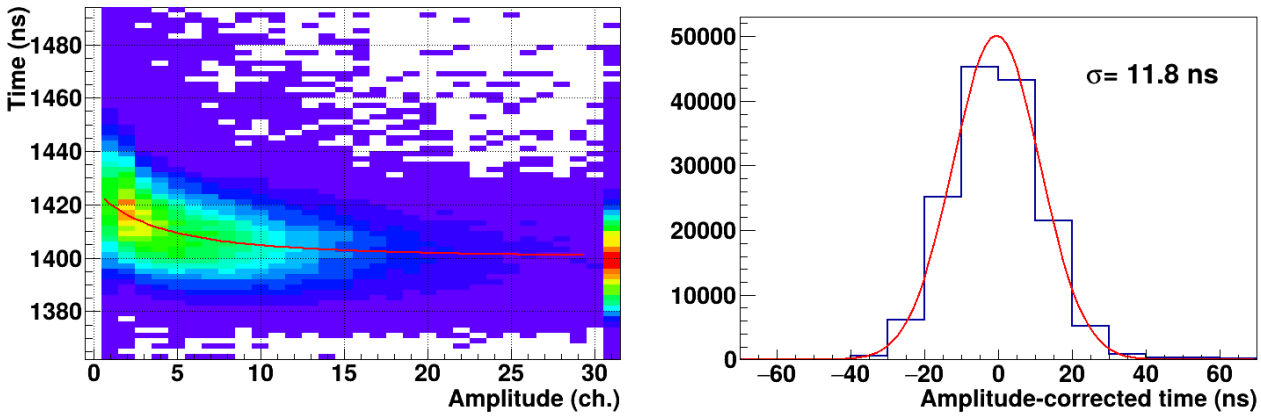


Figure 5. VSP hit-time response. (a) Measured hit time as a function of signal amplitude before the time-slewing correction. The red curve shows the fitted parameterization used to derive the amplitude-dependent correction. (b) Distribution of the corrected VSP hit time relative to the trigger pulse. A Gaussian fit gives $\sigma_t = 11.8$ ns.

3.1.2. Amplitude measurement and signal-to-noise ratio

The cluster signal-to-noise ratio (SNR) was studied for VSP hits associated with local SiBT-target–VSP–GEM1 track candidates in the calibration dataset recorded without magnetic field (See Sec.2.3). Cluster amplitudes were converted to charge using module- and side-dependent calibration constants. The calibration procedure for the SMX-based silicon readout is described

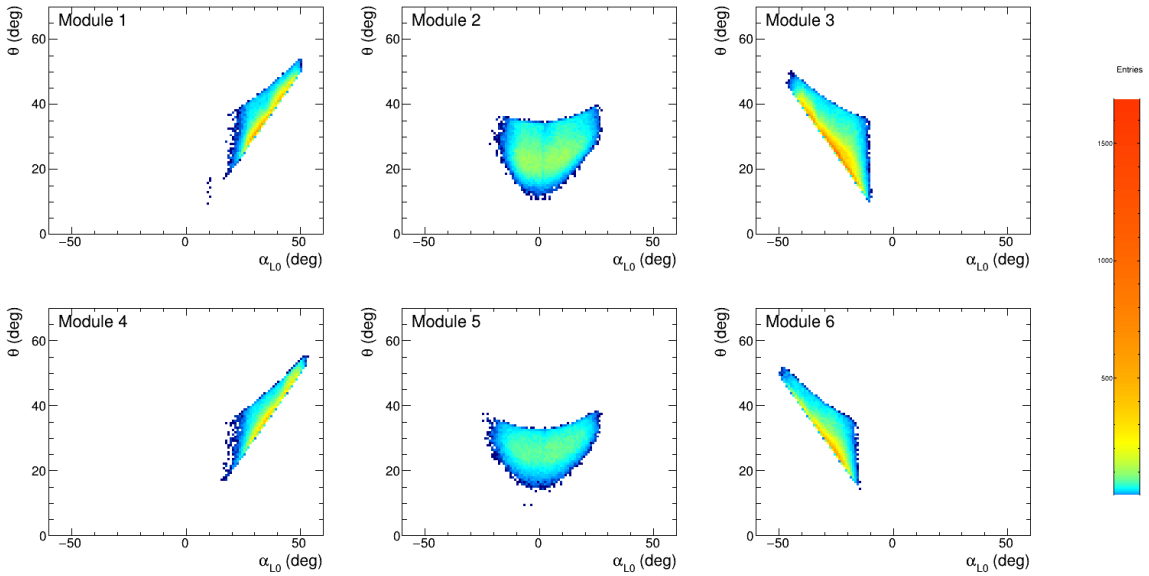


Figure 6. Module-resolved angular coverage of reconstructed tracks in the θ–α_{L0} plane. The angular definitions are given in Sec. 2.3.

in Ref. [17]. Measurements of the internal calibration circuits for different SMX chips showed an RMS variation of the calibration scale of about 4%.

The six VSP modules cover different regions of the angular phase space. The definitions of the polar angle θ and the track incidence angle α_{L0} are given in Sec. 2.3. Their module-resolved coverage in the θ–α_{L0} plane is shown in Fig. 6.

The two angles affect the detector response in different ways. The polar angle θ determines the particle path length in the silicon, whereas the track incidence angle α_{L0} affects charge sharing across the strips. The different angular coverage of the modules therefore contributes to the observed module dependence of the cluster response.

The cluster signal-to-noise ratio was calculated as

$$\mathrm{SNR} = \frac{S_{\mathrm{cluster}}}{N_{m,s}\sqrt{n_{strips}}}, \tag{1}$$

where S_{cluster} is the sum of the hit-induced charges of the strips forming the cluster, n_{strips} is the number of strips contributing to the cluster, and $N_{m,s}$ is the mean single-strip noise for module m and sensor side s. Clusters in the double-metallization region of the p-side (L1) were excluded from the analysis because of the higher strip noise observed in this region, as discussed in Ref. [8].

Figure 7 summarizes the measured cluster response. The left panel shows the most probable value (MPV) of the SNR distribution for each module and sensor side, obtained from Landau–Gaussian convolution fits. The error bars represent the statistical uncertainties of the fitted MPV values. The right panel shows representative calibrated cluster-charge distributions for module 5.

The fitted SNR MPVs range from 15.5 to 30.1 on the n-side (L0) and from 20.9 to 33.2 on the p-side (L1). The module-to-module variation is consistent with the different angular coverage shown in Fig. 6. Modules 2 and 5 are dominated by compact one- and two-strip

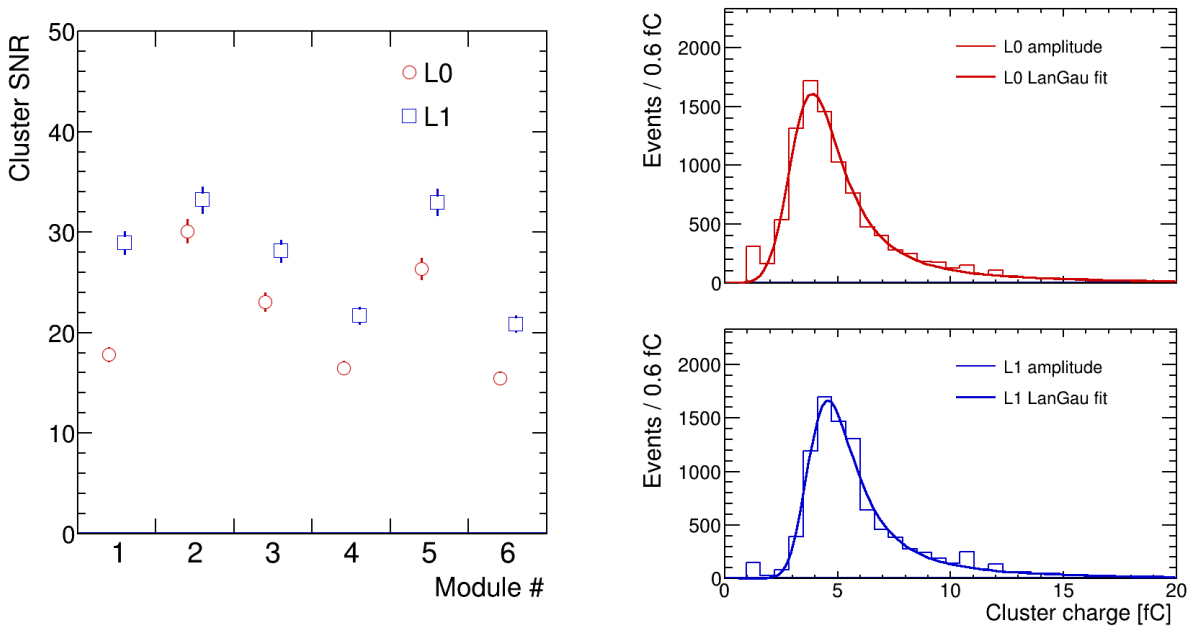


Figure 7. Cluster charge and signal-to-noise response of the VSP. Left: most probable cluster SNR for the six VSP modules and two sensor sides, obtained from Landau–Gaussian convolution fits. The error bars represent the statistical uncertainties of the fitted MPV values. Right: representative calibrated cluster-charge distributions for module 5 with Landau–Gaussian convolution fits.

clusters, whereas larger clusters are more frequent in modules covering broader ranges of track incidence angles. Since the cluster noise increases with the number of strips contributing to the cluster, the different cluster-size composition contributes to the observed SNR variation.

3.1.3. Lorentz drift

For the analysis of data recorded with the nominal magnetic field, the Lorentz drift of charge carriers in the silicon sensors has to be taken into account, since it introduces an additional displacement of the reconstructed hit position. The size of this effect was therefore evaluated directly from the Run 9 data by comparing the detector response in the physics dataset recorded with the nominal magnetic field of 0.5 T with that in the calibration dataset recorded without magnetic field.

The induced signal is described by the Shockley–Ramo theorem [18], according to which the current induced on a given electrode is determined by the carrier motion in the corresponding weighting field. Although both electrons and holes contribute to the total induced signal, the weighting field is concentrated near the collecting strips. Consequently, the n-side (L0) signal is dominated by electrons approaching the n^+ strips, whereas the p-side (L1) signal is dominated by holes approaching the p^+ strips.

A magnetic field deflects the carrier drift direction from the electric-field direction. The Lorentz angle is given by

$$\tan\theta_L = \mu_H B = r_H \mu_d(E,T) B, \tag{2}$$

where μ_d is the drift mobility, r_H is the Hall scattering factor, and B denotes the magnetic-field component perpendicular to the sensor electric field. Electron and hole deflections differ because of their different Hall mobilities.

Figure 8 shows the L0 case in the X–Z projection. For L1, the projected incidence angle α_{L1} is defined analogously in the local U–Z projection. The different L0 and L1 shifts follow

from Eq. (2), because the electron and hole Lorentz angles, θ_L^e and θ_L^h, are different.

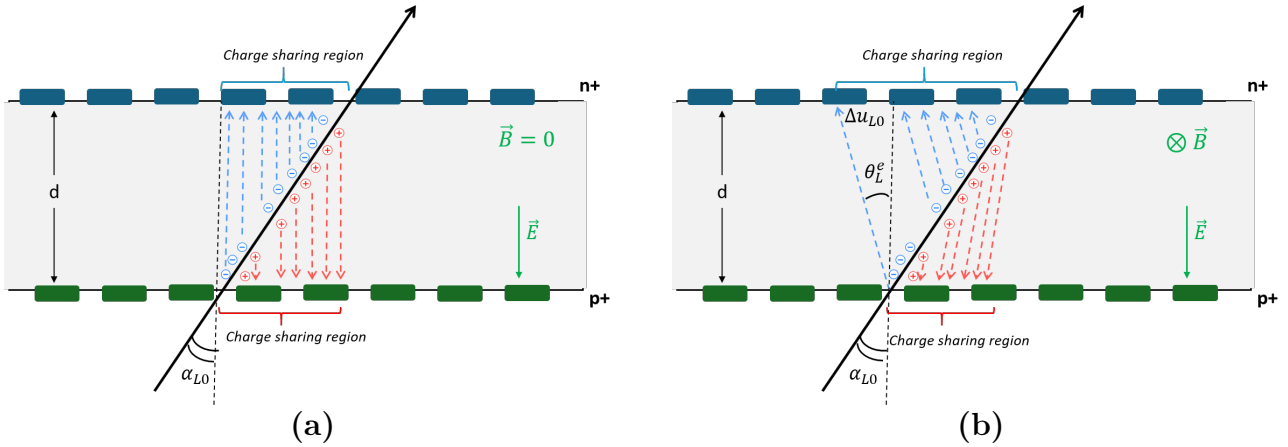


Figure 8. Schematic view of charge-carrier drift in a double-sided silicon strip sensor without (a) and with (b) magnetic field. It does not include diffusion, strip-weighting-field effects, capacitive charge sharing or threshold effects. The scheme is shown for L0 in the X–Z projection; the L1 case is treated analogously in the U–Z projection.

For approximately uniform ionization through a sensor of thickness d, the charge carriers are produced uniformly along the drift direction. For a carrier with drift distance z to the collecting electrode, the Lorentz-induced transverse displacement is $z \tan\theta_L$. Averaging over the sensor thickness gives the corresponding displacement of the charge centroid,

$$|\Delta u_{\mathrm{CoG}}| \simeq \frac{1}{d}\int_0^d z \tan|\theta_L|\, dz = \frac{d}{2}\tan|\theta_L|. \tag{3}$$

The absolute cluster size depends on several detector-response effects, including diffusion, non-uniform weighting fields near the strips, capacitive charge sharing and thresholds. The observable used here is the displacement of the minimum of the measured $\langle N_{\mathrm{strips}}\rangle(\alpha_s)$ curve between the zero-field and magnetic-field data for the same sensor side.

The minimum occurs when the geometrical charge sharing is compensated by the Lorentz deflection of the charge carriers [19]. This makes the method less sensitive to alignment offsets than a direct comparison of mean track–hit residuals.

Modules 5 and 2 were selected for this study because the region around the minimum is well populated for both modules, as shown in Fig. 6. The calibration and physics datasets were fitted separately with

$$\langle N_{\mathrm{strips}}\rangle(\alpha_s) = N_{\mathrm{min}} + a_s(\alpha_s - \alpha_{\mathrm{min},s})^2, \tag{4}$$

where $\alpha_{\mathrm{min},s}$ denotes the fitted minimum. Using the fitted values $\alpha^0_{\mathrm{min},s}$ and $\alpha^B_{\mathrm{min},s}$ for the calibration and physics datasets, respectively, the field-induced shift is defined as

$$\Delta\alpha_s = \alpha^B_{\mathrm{min},s} - \alpha^0_{\mathrm{min},s}, \qquad s = L0, L1.$$

The module 5 results are shown in Fig. 9.

The measured shifts are $\Delta\alpha_{L0} = (-3.2 \pm 0.3)^\circ$ and $\Delta\alpha_{L1} = (-0.3 \pm 0.4)^\circ$. Interpreting the shifts of the cluster-size minima as Lorentz-angle estimates, $|\theta_L| \simeq |\Delta\alpha_s|$, Eq. 3 gives

$$|\Delta u_{\mathrm{CoG},L0}| = (9.0 \pm 0.8)\ \mu\mathrm{m}, \qquad |\Delta u_{\mathrm{CoG},L1}| = (0.8 \pm 1.1)\ \mu\mathrm{m}.$$

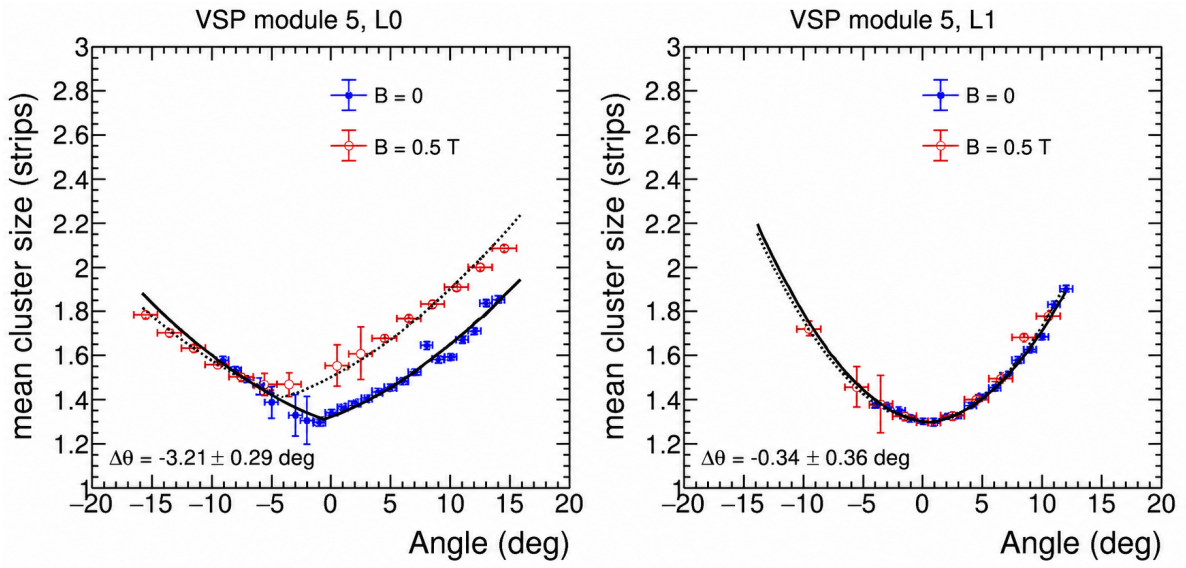


Figure 9. Mean cluster size as a function of the track incidence angle for the n-side (L0) and p-side (L1) of VSP module 5. The calibration dataset recorded without magnetic field is compared with the physics dataset recorded with the nominal magnetic field. The curves show parabolic fits around the minima.

Applying the same procedure to module 2 gives $\Delta\alpha_{L0} = (-3.7 \pm 0.4)°$, consistent with the result for module 5.

For all modules, the magnetic-field component perpendicular to the sensor electric field is $B \simeq 0.5$ T. For a sensor temperature of 25°C, a nominal bias voltage of 100 V, and a sensor thickness of $d = 320$ μm, the mobility model of Ref. [20] gives $\theta_L^e = 3.7°$ and $\theta_L^h = 0.9°$. Equation 3 then gives expected charge-centroid shifts of 10.5 μm for electrons and 2.4 μm for holes.

The measured n-side (L0) result agrees with the predicted electron Lorentz angle. The smaller p-side (L1) shift is consistent with the lower hole Hall mobility and is also compatible with zero within the present uncertainty.

3.2. Tracking performance

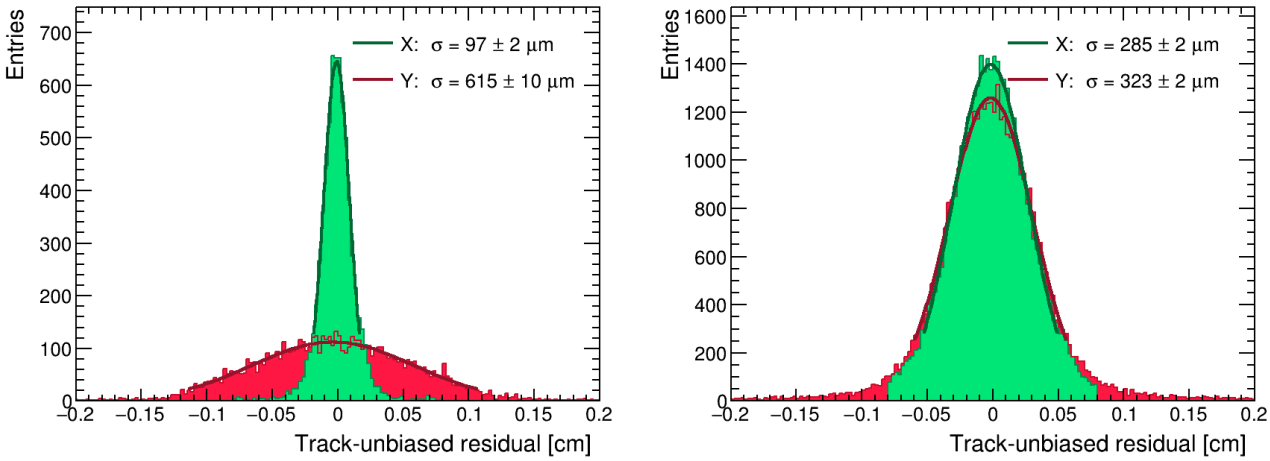
3.2.1. Track–hit residuals

Track–hit residuals were measured in the calibration dataset recorded without magnetic field using two independent linear reference configurations, one based on the FSD stations and one on the GEM stations. The VSP hit was excluded from both reference-track fits.

The residuals are defined as $\Delta X = X_{\mathrm{VSP}} - X_{\mathrm{pred}}$ and $\Delta Y = Y_{\mathrm{VSP}} - Y_{\mathrm{pred}}$, where X_{pred} and Y_{pred} are the reference-track coordinates extrapolated to the VSP plane. Reference tracks were required to satisfy $\chi^2/\mathrm{ndf} < 1.5$.

Figure 10 shows the resulting unbiased track–hit residuals. The standard deviations of Gaussian fits to the central part of the distributions are $\sigma_X = (97 \pm 2)$ μm and $\sigma_Y = (615 \pm 10)$ μm for the FSD reference, and $\sigma_X = (285 \pm 2)$ μm and $\sigma_Y = (323 \pm 2)$ μm for the GEM reference.

The two reference configurations have different extrapolation precisions. The FSD reference provides better precision in X, whereas the GEM reference gives more similar resolutions in the two coordinates. The measured residual widths are dominated by the reference-track



(a) (b)

Figure 10. Unbiased track–hit residuals measured in the calibration dataset recorded without magnetic field. (a) Linear reference track based on the FSD stations. (b) Linear reference track based on the GEM stations. The VSP hit is excluded from both reference fits. The solid curves show Gaussian fits to the central region of the distributions.

extrapolation uncertainty and therefore do not represent the intrinsic spatial resolution of the VSP.

A head–tail cluster-position estimator was also tested as an alternative to the standard center-of-gravity (CoG) method for large track incidence angles [19]. A small improvement of about 1 μm was observed, which is negligible compared with the residual widths and is consistent with their being dominated by the reference-track extrapolation uncertainty.

3.2.2. Hit-matching efficiency

The VSP hit-matching efficiency was measured in the calibration dataset recorded without magnetic field using the two independent FSD- and GEM-based reference configurations described in Sec. 3.2.1. A compatible VSP hit was selected using the normalized track–hit distance

$$d_R = \sqrt{\left(\frac{\Delta X}{\sigma_X}\right)^2 + \left(\frac{\Delta Y}{\sigma_Y}\right)^2}, \tag{5}$$

where the reference-specific values of σ_X and σ_Y were obtained from the residual distributions described in Sec. 3.2.1. The nominal matching requirement was $d_R < 5$.

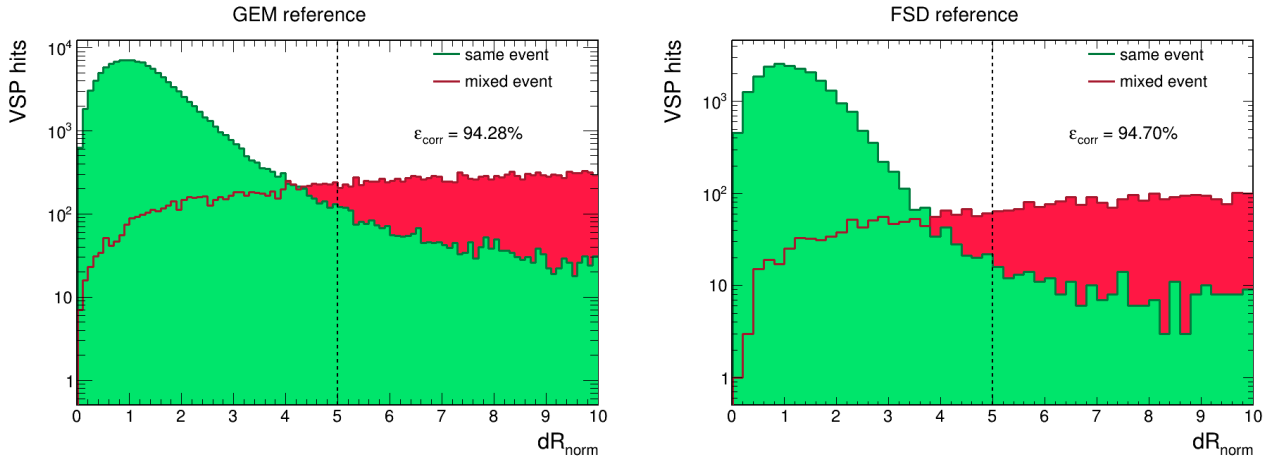
To suppress edge effects, only reference tracks crossing the VSP sensitive area at least 5 mm from its edges were retained. The hit-matching efficiency was defined as $\varepsilon = N_{\mathrm{matched}}/N_{\mathrm{tracks}}$, where N_{tracks} is the number of independently reconstructed reference tracks crossing the selected fiducial region and N_{matched} is the number of those tracks with a compatible VSP hit.

Because of the relatively high VSP hit occupancy, accidental matches between reference tracks and VSP hits can occur. Their contribution was estimated using event mixing. The same reference tracks were matched to VSP hits taken from different events using the same geometrical and matching criteria. The corrected efficiency was calculated as

$$\varepsilon_{\mathrm{corr}} = \frac{\varepsilon_{\mathrm{same}} - \varepsilon_{\mathrm{mix}}}{1 - \varepsilon_{\mathrm{mix}}}, \tag{6}$$

where $\varepsilon_{\mathrm{same}}$ and $\varepsilon_{\mathrm{mix}}$ are the matching probabilities for the same-event and mixed-event samples, respectively. The statistical uncertainty on $\varepsilon_{\mathrm{corr}}$ was obtained by propagating their binomial uncertainties.

Figure 11 shows the same-event and mixed-event d_R distributions. Both reference configurations show a clear excess of same-event matches at small d_R.



(a) (b)

Figure 11. Normalized VSP track–hit matching distance for (a) the GEM reference and (b) the FSD reference. Green distributions correspond to VSP hits from the same event, while red distributions show the mixed-event control sample used to estimate accidental track matching. The dashed line indicates the nominal requirement $d_R < 5$.

Table 2. Integrated VSP hit-matching efficiency obtained with the two independent reference configurations. The uncertainty quoted for $\varepsilon_{\mathrm{corr}}$ is statistical.

Reference	$\varepsilon_{\mathrm{same}}$, %	$\varepsilon_{\mathrm{mix}}$, %	$\varepsilon_{\mathrm{corr}}$, %
GEM reference	94.6	5.5	94.3 ± 0.1
FSD reference	94.9	4.4	94.7 ± 0.2

As summarized in Table 2, the two independent reference configurations give consistent corrected VSP hit-matching efficiencies of about 95% in the selected fiducial region. For comparison, dedicated proton-beam tests of the same DSSD technology demonstrated detection efficiencies above 99% in fully operational sensor regions [8].

3.3. Contribution of the VSP to BM@N tracking

3.3.1. Track impact parameter

Precise determination of decay vertices is crucial for the reconstruction of complex decay topologies. The contribution of the near-target VSP measurement to the vertexing performance was evaluated using the track impact parameter, defined as the transverse distance of closest approach of the particle trajectory to the primary vertex. In the present analysis, its x and y projections were studied as a function of the inverse rigidity q/p.

Two samples of CTS tracks were compared. *VSP-start tracks* have their first reconstructed tracking point in the VSP, whereas *FSD1-start tracks* begin in FSD1, the first tracking station

downstream of the VSP. Tracks were required to be associated with the reconstructed primary vertex and to satisfy $\theta > 25°$.

The width of the impact-parameter distributions was characterized by σ, defined as the half-width of the central 68% interval of the corresponding distribution. The result is shown in Fig. 12.

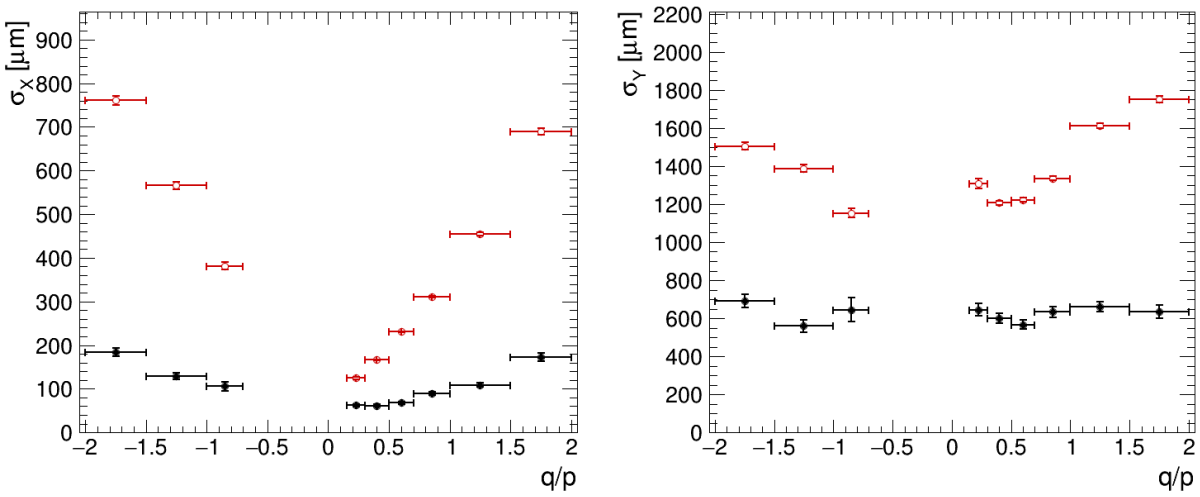


Figure 12. Half-width σ of the central 68% interval of the x- and y-projected track impact-parameter distributions as a function of the inverse rigidity q/p. Solid (black) markers show VSP-start tracks, while open (red) markers show FSD1-start tracks. The left and right panels correspond to the x and y projections, respectively.

In all cases VSP-start tracks show narrower impact-parameter distributions over the studied q/p range. The difference is most pronounced in the x (bending) projection, where the widths for the VSP-start sample are approximately 50–200 μm. Smaller widths are also observed in the y projection.

3.3.2. Rigidity reconstruction with VSP–GEM tracklets

The large geometrical overlap of the VSP with the first GEM stations makes it possible to construct short VSP–GEM tracklets in a region where the acceptance of the CTS is reduced. This topology is of particular interest for extending the reconstruction of high-p_T protons towards midrapidity.

The potential extension of the tracking acceptance was first evaluated using DCM–SMM Monte Carlo simulations of minimum-bias Xe+Sn collisions at 3 AGeV in the BM@N Run 9 geometry [21]. A dedicated reconstruction-level study of this VSP-assisted topology, including magnetic-field propagation and combinatorial-background suppression, is presented in Ref. [22].

The phase space of reconstructible primary protons was compared for CTS tracks and VSP–GEM tracklets. A proton was considered reconstructible by the CTS if MC points were present in at least four distinct FSD or GEM stations. For the VSP–GEM topology, reconstructibility required MC points in the VSP, GEM1, and GEM2 together with the three-dimensional primary-vertex point. Since this study is based on MC information rather than reconstructed detector hits, it represents geometrical reconstructability rather than tracking efficiency.

Figure 13 shows the resulting acceptance for the 0–30% centrality class in the (y, p_T) plane, where y denotes the proton rapidity relative to the center-of-mass rapidity, $y = y_{\mathrm{lab}} - y_{\mathrm{cm}}$; the proton mass is used in the rapidity calculation. The VSP–GEM tracklet topology extends the

reconstructible phase space towards midrapidity and higher transverse momenta. For primary protons with $p_T > 1.2$ GeV/c, the geometrical reconstructability increases from 34.7% for the CTS alone to 43.1% when the VSP–GEM tracklet topology is included. This corresponds to an absolute gain of about 8.5 percentage points, or a relative increase of about 24% with respect to the CTS.

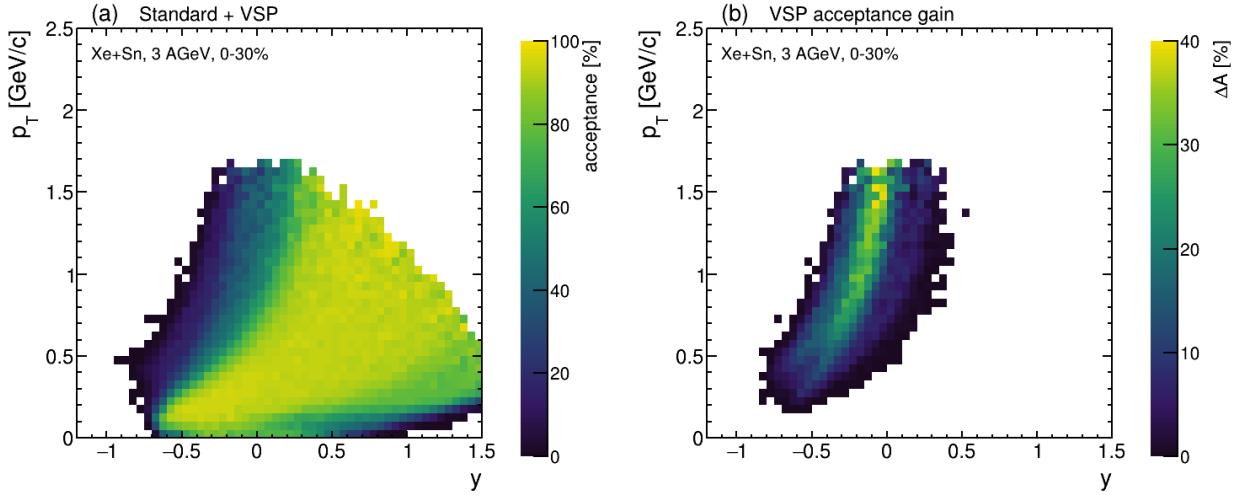


Figure 13. Monte Carlo geometrical reconstructability of primary protons in Xe+Sn collisions at 3 AGeV for the 0–30% centrality class in the (y, p_T) plane, where y is the proton rapidity relative to the center-of-mass rapidity, $y = y_{\mathrm{lab}} - y_{\mathrm{cm}}$. (a) Acceptance of the combined CTS and VSP–GEM tracklet configurations. (b) Absolute increase $\Delta A = A_{\mathrm{CTS+VSP\text{-}GEM}} - A_{\mathrm{CTS}}$ provided by the VSP–GEM tracklets. The acceptance in each bin is defined as the fraction of generated primary protons satisfying the corresponding MC-point reconstructability requirement.

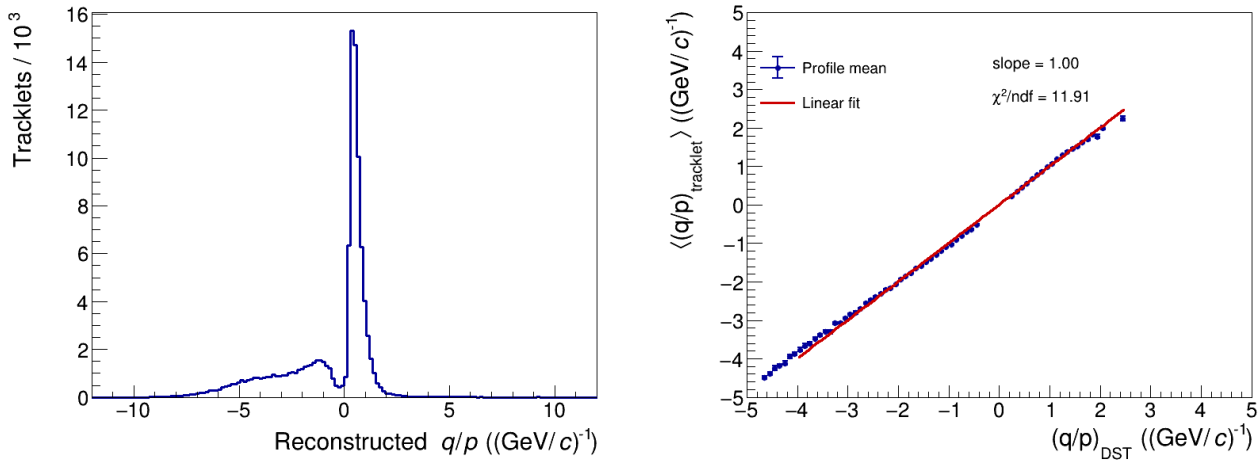
Motivated by this geometrical acceptance gain, VSP–GEM tracklets were reconstructed in the physics dataset recorded with the nominal magnetic field. The tracklets were built using the three-dimensional primary-vertex point, one VSP hit, and measurements in the first two GEM stations. The inverse rigidity q/p was determined using the BM@N magnetic-field map.

Figure 14(a) shows the reconstructed q/p distribution. For validation, the VSP–GEM tracklets were matched to CTS tracks reconstructed in the same events. Figure 14(b) shows the correlation between the two q/p estimates. A linear fit to the correlation gives a slope consistent with unity.

This demonstrates that VSP–GEM tracklets provide a reliable inverse-rigidity estimate in the region where they overlap with the CTS. Their larger geometrical acceptance makes this approach promising for extending track reconstruction towards the phase-space region not fully covered by the CTS.

4. Conclusion

The Vertex Silicon Plane was commissioned and operated for the first time during BM@N Run 9 as the tracking station closest to the target. Successful integration of the free-streaming VSP data into the BM@N data stream was demonstrated by the time coincidence of VSP hits with the trigger and their spatial matching with reconstructed tracks. The detector showed stable in situ performance, with the most probable cluster SNR values ranging from 15.5 to 33.2 and an amplitude-corrected hit-time distribution with a width of about 12 ns. In the nominal



(a) (b)

Figure 14. Rigidity reconstruction with VSP–GEM tracklets in the physics dataset recorded with the nominal magnetic field. (a) Distribution of the reconstructed inverse rigidity q/p. (b) Correlation between the q/p values reconstructed with the VSP–GEM tracklets and CTS tracks; the slope of the linear fit is consistent with unity.

magnetic field of the SP-41 magnet, the Lorentz drift of charge carriers leads to a displacement of the reconstructed cluster position. For module 5, the measured charge-centroid shift is about 9 μm on the n-side, while the corresponding p-side shift is compatible with zero within the present uncertainty. The measured Lorentz angle provides the basis for correcting this displacement in the reconstructed hit position.

The tracking performance was studied using independent FSD- and GEM-based reference tracks. Both reference samples give consistent VSP hit-matching efficiencies of about 95%. The track–hit residuals show good agreement between VSP hits and the extrapolated reference tracks.

The contribution of the VSP to the performance of the CTS was also studied. It was shown that the VSP improves the transverse track impact-parameter resolution, particularly in the x (bending) projection. Monte Carlo studies show that the VSP–GEM tracklet topology extends the geometrical reconstructability beyond the CTS acceptance. For primary protons with $p_T > 1.2$ GeV/c in the 0–30% centrality class, the gain is about 8.5 percentage points, corresponding to an increase of about 24% relative to the CTS. In the physics data, VSP–GEM tracklets provide an inverse-rigidity estimate consistent with that obtained from CTS tracks.

Thus, the VSP not only operated successfully as an additional silicon tracking station, but also extends the BM@N tracking capabilities towards larger polar angles and the midrapidity region. Further Monte Carlo reconstruction studies are required to quantify the tracking efficiency in the extended acceptance and to demonstrate the full reconstruction capabilities of the VSP–GEM tracklet approach.

Author contributions

D. Dementev: conceptualization, project coordination, methodology, formal analysis, data curation, detector commissioning and operation during Run 9, supervision, writing – original draft.

M. Shitenkov: readout electronics, calibration, electronics testing, detector commissioning and operation during Run 9.

A. Kolozhvari: software, data curation, integration of the VSP data stream into the BM@N event builder, detector commissioning and operation during Run 9.

V. Leontyev: online data monitoring, data processing, detector commissioning and operation during Run 9.

A. Sheremetev: assembly of the silicon detector modules and the VSP station, installation and detector commissioning.

D. Andreev: methodology, mechanical design of the VSP station, installation and detector commissioning.

R. Arteche Diaz: firmware development and readout synchronization for the VSP.

D. Baranov: software, development of the VSP hit producer and Monte Carlo detector model.

C. Ceballos Sanchez: writing – review and editing.

I. Gabdrakhmanov: software, integration of VSP monitoring histograms into the BM@N online monitoring system.

I. Gorelikov, S. Reyes Peña and E. Tsapulina contributed to detector operation during Run 9.

T. Lygdenova: installation, detector commissioning and operation during Run 9.

Yu. Murin: project administration, supervision.

I. Osokin: slow-control system.

I. Rufanov: methodology, formal analysis, alignment studies, writing – review and editing.

A. Voronin: fabrication of carbon-fiber structural components, detector commissioning and operation during Run 9.

Acknowledgements

The authors thank Sergey Novozhilov and Semyon Piyadin, Technical Coordinator of the BM@N experiment, for their assistance during the installation and commissioning of the VSP.

The authors are grateful to the BM@N DAQ team for their support and for providing equipment used during the development and debugging of the VSP integration into the BM@N data-acquisition system.

The authors also thank Konstantin Gertsenberger, Alexandr Zinchenko, Nikolay Zamyatin, and Mikhail Kapishin for valuable discussions, as well as the BM@N software and data-analysis group for support with reconstruction and analysis software.

The JINR accelerator team is acknowledged for their support during Run 9 operation.

Funding

This work was supported by the Joint Institute for Nuclear Research (JINR) and the BM@N collaboration.

Conflicts of Interest

The authors declare that they have no conflicts of interest.

Additional Information

Use of artificial intelligence. During the preparation of this manuscript, the authors used OpenAI for language editing, improvement of text structure, and stylistic revision. All scientific content, experimental results, data analysis, and conclusions were produced and verified by the authors. The AI-assisted text was reviewed and edited by the authors, who take full responsibility for the content of the article.

References

[1] P. Senger, D. Dementev, J. Heuser, M. Kapishin, E. Lavrik, Yu. Murin, A. Maksymchuk, H. R. Schmidt, C. Schmidt, A. Senger, A. Zinchenko, Upgrading the Baryonic Matter at the Nuclotron Experiment at NICA for Studies of Dense Nuclear Matter, Particles **2** (2019) 481–490. doi:10.3390/particles2040029.

[2] BM@N Collaboration, The BM@N spectrometer at the NICA accelerator complex, Nuclear Instruments and Methods in Physics Research Section A **1065** (2024) 169532. doi:10.1016/j.nima.2024.169532.

[3] D. Chemezov, M. Kapishin, S. Khabarov, Yu. Kopylov, E. Martovitsky, S. Novozhilov, S. Piyadin, S. Sedykh, E. Streletskaya, O. Tarasov and N. Zamyatin, *Beam tracker system for the BM@N/NICA experiment*, PoS **TIPP2023** (2025) 124. doi:10.22323/1.468.0124.

[4] A. D. Sheremetev, V. V. Leontiev, D. V. Dementev, M. O. Shitenkov, Yu. A. Murin, Technological Process of Assembly and QA Testing of Silicon Tracking Modules with Silicon Strip Sensor, Physics of Particles and Nuclei Letters **21** (2024) 466–480. doi:10.1134/S1547477124700456.

[5] A. D. Sheremetev, *Development and fabrication of tracking modules based on double-sided silicon microstrip detectors*, Candidate of Technical Sciences thesis, Joint Institute for Nuclear Research, Dubna, Russia, 2025, in Russian, https://dissertations.jinr.ru/ru/Dissertations/Announcement/236.

[6] K. Kasinski, A. Rodriguez-Rodriguez, J. Lehnert, W. Zubrzycka, R. Szczygiel, P. Otfinowski, R. Kleczek, C. J. Schmidt, Characterization of the STS/MUCH-XYTER2, a 128-channel time and amplitude measurement IC for gas and silicon microstrip sensors, Nuclear Instruments and Methods in Physics Research Section A **908** (2018) 225–235. doi:10.1016/j.nima.2018.08.076.

[7] D. V. Dementev, A. D. Sheremetev, M. O. Shitenkov, V. V. Leontiev, I. A. Rufanov, Yu. A. Murin, Characterization of Tracking Modules Based on DSSD Sensors at the SC-1000 Accelerator for the BM@N Project, Physics of Particles and Nuclei Letters **21** (2024) 919–927. doi:10.1134/S1547477124701000.

[8] D. Dementev, R. Arteche Diaz, C. Ceballos Sanchez, A. Kolozhvari, V. Leontyev, N. Maltsev, Yu. Murin, A. Rodriguez Alvarez, I. Rufanov, A. Sheremetev, M. Shitenkov, V. Zherebchevsky, In-beam tests of double-sided silicon strip detector modules for the BM@N experiment, Nuclear Instruments and Methods in Physics Research Section A **1075** (2025) 170390. doi:10.1016/j.nima.2025.170390.

[9] D. Dementev, M. Gumiński, I. Kovalev, M. Kruszewski, I. Kudryashov, A. Kurganov, P. Miedzik, Yu. Murin, K. Poźniak, C. J. Schmidt, M. Shitenkow, A. G. Voronin, W. M. Zabołotny, Fast Data-Driven Readout System for the Wide Aperture Silicon Tracking System of the BM@N Experiment, Physics of Particles and Nuclei **52** (2021) 830–834. doi:10.1134/S1063779621040213.

[10] D. Dementev, D. Andreev, A. Kolozhvari, V. Leontyev, M. Shitenkov, A. Sheremetev, Yu. Murin, Silicon Tracking Station with a Streaming Readout as a Part of the BM@N Tracking System, Physics of Particles and Nuclei **57** (2026) 379–383. doi:10.1134/S1063779625701424.

[11] M. Al-Turany, D. Bertini, R. Karabowicz, D. Kresan, P. Malzacher, T. Stockmanns, F. Uhlig, The FairRoot framework, Journal of Physics: Conference Series **396** (2012) 022001. doi:10.1088/1742-6596/396/2/022001.

[12] D. A. Zinchenko, E. G. Nikonov, A. I. Zinchenko, R. A. Zinchenko, Development of the Vector Finder Toolkit for Track Reconstruction in the BM@N Experiment, Physics of Particles and Nuclei Letters **21** (2024) 544–552. doi:10.1134/S1547477124700560.

[13] D. Baranov, P. Batyuk, K. Gertsenberger, S. Merts, Track Reconstruction in the BM@N Experiment, EPJ Web of Conferences **226** (2020) 03003. doi:10.1051/epjconf/202022603003.

[14] R. A. Zinchenko, J. R. Drnoyan, M. N. Kapishin, I. A. Rufanov, V. A. Vasendina, A. I. Zinchenko, D. A. Zinchenko, Reconstruction of Decays of Strange Particles Produced in Xe + CsI Interactions with the BM@N Detector, Physics of Particles and Nuclei Letters **22** (2025) 1250–1261. doi:10.1134/S1547477125701535.

[15] I. A. Rufanov, *Report on GEM and silicon alignment in Run 9*, BM@N internal technical report, JINR, 10 August 2026, in Russian, unpublished.

[16] I. A. Rufanov, *Rotations of silicon modules around the beam axis*, BM@N internal technical report, JINR, 11 August 2026, in Russian, unpublished.

[17] M. O. Shitenkov, *Streaming Data Acquisition System for the Silicon Tracking System*, Candidate of Technical Sciences thesis, Joint Institute for Nuclear Research, Dubna, Russia, 2026, in Russian, https://dissertations.jinr.ru/ru/Dissertations/Announcement/328

[18] W. Shockley, Currents to Conductors Induced by a Moving Point Charge, Journal of Applied Physics **9** (1938) 635–636. doi:10.1063/1.1710367.

[19] ATLAS SCT Collaboration, Beam tests of ATLAS SCT silicon strip detector modules, Nuclear Instruments and Methods in Physics Research Section A **538** (2005) 384–407. doi:10.1016/j.nima.2004.08.133.

[20] T. Lari, Lorentz angle variation with electric field for ATLAS silicon detectors, ATLAS Note ATL-INDET-2001-004, CERN, Geneva, Switzerland, 2001, https://cds.cern.ch/record/684187,

[21] M. Baznat, A. Botvina, G. Musulmanbekov, V. Toneev, V. Zhezher, Monte-Carlo generator of heavy ion collisions DCM-SMM, Physics of Particles and Nuclei Letters **17** (2020) 303–324. doi:10.1134/S1547477120030024.

[22] D. Dementev, D. Baranov, V. Leontyev, Yu. Murin, I. Rufanov, *Extending the BM@N tracking acceptance toward midrapidity with the Vertex Silicon Plane*, preprint, 2026.